Modeling pore fluid pressure and deformation in unsaturated soils under gravitational compaction and cyclic loading

Nan-Chieh Chao¹, Ronaldo I. Borja¹, WeiCheng Lo^{2,*}, Chuen-Fa Ni³, Jhe-Wei Lee²

Summary. Cyclic loading of fluid-bearing soils often induces excess pore water pressure leading to accumulation of strain in the solid matrix. Additionally, variations in material density and volumetric fraction due to gravitational effects create momentum forces, subsequently causing deformation in the soil. In this paper, we present a mathematical framework of poroelasticity that generalizes the simultaneous action of gravitational body forces and cyclic loading for analyzing solid deformation and fluid pressure dissipation in partially-saturated porous media. We numerically solve a mixed strain-controlled and pressure-prescribed boundary-value problem using the finite difference scheme as a representative example to examine the impact of gravity forces quantitatively. Our results indicate that gravitational compaction impacts both the total settlement and excess pore water pressure, and that its effect is particularly pronounced at lower water saturations irrespective of the excitation frequency, soil length, and soil type. Gravity effect is more significant in soils with a higher compressibility, but appears to be insensitive to the excitation frequency. Notably, gravitational effect correlates linearly with depth of the soil deposit, and thus, it should be incorporated into the consolidation theory of poroelasticity.

Keywords. Cyclic load; fluid pressure; gravitational compaction; poroelasticity; solid deformation

1 Introduction

Accurate description of the strong hydro-mechanical coupling in an elastic matrix with immiscible fluids permeating through a network of interconnected

¹Department of Civil and Environmental Engineering, Stanford University, Stanford, CA 94305, USA.

²Department of Hydraulic and Ocean Engineering, National Cheng Kung University, Tainan, 701, Taiwan.

³Graduate Institute of Applied Geology, National Central University, Taoyuan City, 32001, Taiwan.

^{*}E-mail: lowc@mail.ncku.edu.tw

pore spaces has long been a central issue in a wide range of relevant disciplines. Coupled phenomena are very common in problems such as land subsidence caused by groundwater abstraction [34], slope failure induced by rainfall [8–10, 18], dynamic soil-fluid-structure interaction due to seismic events [12], oil recovery enhanced by seismic wave stimulation [26, 41], and changes in fracture permeability triggered by reservoir production [49], among others. There is now a broad consensus that many engineering applications can be comprehensively understood only when the intricate hydromechanical coupling between the solid skeleton and the interstitial fluids, now known as poroelasticity, is thoroughly taken into account.

Biot [1, 2, 4] presented a unified mathematical framework within the thermodynamically-based context that enables simultaneous modeling of deformation of the solid skeleton and flow of fluid through the pore spaces. His formulation applies to a homogeneous and fully saturated porous medium in which the solid deformation impacts the fluid flow and vice versa. Since then, many scholars have made contributions further advancing the theory to variably-saturated porous media. Numerous papers have focused on identifying an effective stress measure for single-porosity [11, 38, 39] and double-porosity [7, 15] media, as well as for anisotropic geologic materials [46–48]. Because of the general nature of these theories, analytical solutions are difficult to find, but many of them have found their way into computer codes.

A generalized Biot formulation that includes an extension of the constitutive equations for porosity changes and the linearized increment of fluid content to a two-fluid system was presented by Lo and co-workers [22, 23, 27] employing the continuum theory of mixtures [40]. The linearized fluid content is a crucial poroelasticity parameter that characterizes the fractional volume of fluids flowing in or out of a given volume element attached to the solid frame in response to an applied stress; therefore, it involves the solid frame contraction and the differences in intrinsic volumetric strain between the solid and each of the fluids [22, 23]. These poroelasticity models feature partial differential equations that are coupled through physical terms describing inertial coupling, viscous damping, and applied stresses. Inertial coupling arises from the acceleration differences between the fluid phases and the solid matrix, whereas viscous damping results from their relative velocity. Hence, exact decoupling of model equations is required to obtain closed-form, analytical solutions. This was achieved by Lo et al. [25], yielding three Helmholtz equations featuring complex-valued, frequency-dependent normal coordinates that correspond physically to three independent kinematical modes.

The poroelastic response of a fluid-bearing medium to cyclic loading is quite different from the more typical response of the same medium to a time-invariant load. Lo et al. [29, 35] and Deng et al. [16] considered cyclic loading in their formulations by using the technique of Laplace transformation and developed a set of closed-form analytical solutions that contain the individual frequency-independent and frequency-dependent components of the poroelastic response. Their solutions apply to quasi-static loading where inertia effects

may be ignored. Analytical solutions elucidating the transient deformationflow mechanism of a vertical, dual-layered poroelastic system with an upper unsaturated layer and a lower saturated layer under constant loading were derived by Lo et al. [31, 32] illustrating the effects of two vastly different boundary conditions. Lo et al. [28, 33], established a physically-consistent approach examining changes in the poroelastic behavior as different fluid fluxes occur across the boundary surface.

However, geological sediments may undergo compaction under their own weight caused by gravitational body forces, resulting in a reduction in volumetric fraction of each phase and a change in its material density. This mechanical process is termed gravitational compaction, which has been conventionally neglected in the theory of poroelasticity; yet, gravity force is shown to be capable of creating additional momentum exchange. Gibson et al. [20] conducted a numerical analysis of the nonlinear consolidation behavior of a saturated compressible soil and concluded that neglecting the body forces could result in underestimating the excess pore water pressure due to different behaviors occurring for the relationship between void ratio and effect stress. This oversight has the potential to cause design failures due to the overestimation of shear strength. Recent studies have further underscored the crucial role of accounting for body forces for an accurate modeling of the rate of consolidation and the resulting total settlement in both saturated and unsaturated porous media [17, 19, 44, 45].

Chao et al. [14] incorporated gravity loading into the model equations of poroelasticity [28]. The dissipation of excess pore water pressure and the temporal evolution of the total settlement in unsaturated soils were evaluated in their study under the condition of a constant load. However, an external cyclic loading could alter the deformation pattern and pore-water pressure response of the soil. To date, few studies have been reported that consider the flow and deformation mechanisms in partially saturated soils incorporating the combined effects of both gravity force and periodic stress perturbations.

The objective of the present effort is to capture the transient solid-fluid interactions in unsaturated porous materials subjected to a harmonic stress compression and relaxation utilizing the theory of poroelasticity [14], while also accounting for the momentum exchange resulting from the variations in material density and volumetric fraction due to gravity effects. Our point of departure is the poroelasticity formulation of Lo et al. [30] that accommodates the effect of cyclic loading. The standard finite difference method with the second-order accurate symmetric difference in space and the first-order finite difference in time [13] is used in this work to solve the boundary-value problem for the dependent variables of displacement as well as pore water pressure. Sensitivity studies are conducted to identify parameters that have an important influence on the gravitational compaction, such as water saturation, excitation frequency, soil compressibility, and the thickness of the soil column.

2 Model equations

Employing the theory of poroelasticity [1, 23, 28], Lo et al. [30] developed a set of coupled partial differential equations describing the variation of solid deformation and pore fluid pressure in a homogeneous, isotropic unsaturated soil. The formulation includes the effect of gravitational compaction arising from changes in the volumetric fraction and material density of each constituent under isothermal condition. The conservation equations take the form

$$R_{11} \left[(d_1 - 1) \frac{\partial e}{\partial t} + d_2 \frac{\partial p_1}{\partial t} + d_3 \frac{\partial p_2}{\partial t} \right]$$

$$= \theta_1 \nabla^2 p_1 - \rho_1 \theta_1 d_1 g \frac{\partial e}{\partial z} - \rho_1 \theta_1 d_2 g \frac{\partial p_1}{\partial z} - \rho_1 \theta_1 d_3 g \frac{\partial p_2}{\partial z}, \qquad (1)$$

$$R_{22} \left[(d_4 - 1) \frac{\partial e}{\partial t} + d_5 \frac{\partial p_1}{\partial t} + d_6 \frac{\partial p_2}{\partial t} \right]$$

$$= \theta_2 \nabla^2 p_2 - \rho_2 \theta_2 d_4 g \frac{\partial e}{\partial z} - \rho_2 \theta_2 d_5 g \frac{\partial p_1}{\partial z} - \rho_2 \theta_2 d_6 g \frac{\partial p_2}{\partial z}, \tag{2}$$

and

$$\left(K_b + \frac{4}{3}G\right)\nabla^2 e - \alpha S_1 \nabla^2 p_1 - \alpha S_2 \nabla^2 p_2 + \Theta_s \frac{\partial e}{\partial z} + \Theta_1 \frac{\partial p_1}{\partial z} + \Theta_2 \frac{\partial p_2}{\partial z} = 0, (3)$$

where ρ_{α} denotes the mass density of phase α ; the subscript α pertain to the three immiscible phases ($\alpha = s$: solid; $\alpha = 1$: non-wetting fluid, henceforth termed "air"; $\alpha = 2$: wetting fluid, henceforth termed "water"; θ_{α} signifies the volumetric fraction of phase α , which is a physical indicator representing the total percentage of the volume of phase α relative to the entire volume of all constituents; $e = \nabla \cdot \boldsymbol{u}_s$ is the volumetric strain in the solid skeleton; $\varepsilon_{\xi} = \nabla \cdot \boldsymbol{u}_{\xi} \ (\xi = 1, 2)$ are the volumetric strains in the two fluid phases; $\boldsymbol{u_s}$ and u_{ξ} are the corresponding displacement vectors; p_{ξ} is the excess (incremental gauge) pore pressure of fluid phase ξ ; $R_{\xi\xi} = \theta_{\xi}^2 \eta_{\xi}/k_s k_{r\xi}$ are constitutive coefficients related to viscous drag caused by velocity differences between the solid and fluid phase ξ ; η_{ξ} is the dynamic shear viscosity of fluid phase ξ ; $k_{r\xi}$ is the relative permeability; k_s is the intrinsic permeability of the porous framework; $S_{\xi} = \theta_{\xi}/\phi$ is the relative saturation of the fluid phase ξ ; ϕ is porosity; g is the gravitational acceleration; $\alpha = 1 - K_b/K_s$ represents the Biot-Willis coefficient [3, 43]; G is the shear modulus of elasticity of the porous medium framework; and K_b is the elastic bulk modulus. Equations (1) and (2) are the equations of linear momentum balance for the fluid phase, whereas Equation (3) is the linear momentum balance for the whole system. The closure condition $S_1 + S_2 = 1$ holds for the system, where S_2 is often referred to in the literature as the degree of saturation.

In Equations (1) through (3), d_1 and d_4 are dimensionless poroelasticity parameters, while d_2 , d_3 , d_5 , and d_6 have the units of stress inverse, whose

physical representation in terms of directly measurable variables is detailed in Appendix A. Furthermore, the gravity parameters Θ_{α} are given by the equations

$$\Theta_s = (\rho_1 \theta_1 d_1 + \rho_2 \theta_2 d_4 + \rho_s \theta_s) g, \tag{4}$$

$$\Theta_1 = (\rho_1 \theta_1 d_2 + \rho_2 \theta_2 d_5) g, \tag{5}$$

and

$$\Theta_2 = (\rho_1 \theta_1 d_3 + \rho_2 \theta_2 d_6) g. \tag{6}$$

It should be noted that because of the existence of gravitational body forces, the total stress does not remain constant, contrary to the conventional theory of poroelasticity under a time-invariant compaction force, but rather increases with a depth in soil thickness. This may in turn lead to variations in material parameters. However, the deformations are considered small enough that the infinitesimal elastic assumption is valid. Therefore, all physical coefficients in Equations (1) through (3) are evaluated in the reference configuration, since we are dealing with an elastic porous medium undergoing small deformations, the central problem in the theory of poroelasticity [2, 4]. Thus, the value of a physical property induced in the current (deformed) configuration is equal to the value in the reference configuration (denoted by a superscript 0) plus the difference between the current and reference values (denoted by capital delta Δ); e.g. the relative saturation of water S_2 in the current configuration is determined by $S_2 = S_2^0 + \Delta S_2$. It follows that in the small-strain regime, it is accurate to neglect the second-order terms in Equation (3), such as $\alpha \Delta S_2 \nabla^2 p_2$, i.e. only the first-order terms (e.g. $\alpha S_2^0 \nabla^2 p_2$) being retained. The difference in relative saturation of water evaluated between the current and reference configurations, ΔS_2 , is a function of capillary pressure [23]: $\Delta S_2 = \frac{dS_1}{dp_c}(p_2 - p_1)$, where $p_c = p_1 - p_2$ is the capillary pressure; $\frac{dS_1}{dp_c}$ expresses the slope (evaluated in the reference configuration) of the curve relating capillary pressure to the relative saturation of air (or water since $S_1 = 1 - S_2$), i.e., the water retention curve.

Specializing to the 1D constrained deformation case, where $e_{xx} = e_{yy} = 0$, $e = e_{zz} = \partial w/\partial z$, Equations (1) through (3) reduce to

$$(d_{1}-1)\frac{\partial}{\partial t}\left(\frac{\partial w}{\partial z}\right) + d_{2}\frac{\partial p_{1}}{\partial t} + d_{3}\frac{\partial p_{2}}{\partial t}$$

$$= \frac{\theta_{1}}{R_{11}}\left[\frac{\partial^{2} p_{1}}{\partial z^{2}} - \rho_{1}d_{1}g\frac{\partial}{\partial z}\left(\frac{\partial w}{\partial z}\right) - \rho_{1}d_{2}g\frac{\partial p_{1}}{\partial z} - \rho_{1}d_{3}g\frac{\partial p_{2}}{\partial z}\right], \quad (7)$$

$$(d_4 - 1)\frac{\partial}{\partial t} \left(\frac{\partial w}{\partial z}\right) + d_5 \frac{\partial p_1}{\partial t} + d_6 \frac{\partial p_2}{\partial t}$$

$$= \frac{\theta_2}{R_{22}} \left[\frac{\partial^2 p_2}{\partial z^2} - \rho_2 d_4 g \frac{\partial}{\partial z} \left(\frac{\partial w}{\partial z}\right) - \rho_2 d_5 g \frac{\partial p_1}{\partial z} - \rho_2 d_6 g \frac{\partial p_2}{\partial z}\right], \quad (8)$$

$$(K_b + \frac{4}{3}G)\frac{\partial^2}{\partial z^2} \left(\frac{\partial w}{\partial z}\right) - \alpha S_1 \frac{\partial^2 p_1}{\partial z^2} - \alpha S_2 \frac{\partial^2 p_2}{\partial z^2} + \Theta_s \frac{\partial}{\partial z} \left(\frac{\partial w}{\partial z}\right) + \Theta_1 \frac{\partial p_1}{\partial z} + \Theta_2 \frac{\partial p_2}{\partial z} = 0, \tag{9}$$

where w is the component of the solid displacement vector in the vertical z direction. Equations (7) through (9) constitute a mathematical model that provides fundamental insights into the one-dimensional poroelastic behavior of an unsaturated porous medium including the gravity effects.

3 Initial and boundary conditions

Initial and boundary conditions must be specified for the solution of the physical problem described in Equations (7) through (9) to be determined. As an illustrative example for our model problem, let us consider a soil sample with thickness h whose top surface is at z = h and the bottom surface is at z = 0, i.e., the positive z-axis is in the upward direction.

An undrained response occurs when the time-dependent surface load q(t) is suddenly applied at $t=0^+$ so that the water content of the soil sample remains unchanged during the load application process. In other words, no fluid is allowed to flow into or out of the soil element during this short period of time when the load is applied instantaneously. In this case, the initial condition incorporating gravitational compaction can be described mathematically by the following equations [30]:

$$\left. \frac{\partial w}{\partial z} \right|_{(z,0)} = \frac{q(t=0)}{K_v^{(u)}} \exp\left[\frac{II}{K_v^{(u)}} (h-z)\right],\tag{10}$$

$$p_1(z,0) = -\gamma_1 \times q(t=0) \times \exp\left[\frac{\Pi}{K_v^{(u)}} (h-z)\right],\tag{11}$$

and

$$p_2(z,0) = -\gamma_2 \times q(t=0) \times \exp\left[\frac{\Pi}{K_n^{(u)}} (h-z)\right],\tag{12}$$

where γ_1 and γ_2 represent loading efficiencies whose physical representation is given in Equations (21b) and (22b) in Lo et al. [28]; $K_v^{(u)}$ is the undrained vertical bulk modulus [27]; and Π is a parameter related to gravity, defined in Lo et al. [30]. Gravitational compaction introduces an additional momentum source, thereby altering the spatial gradient of solid displacement in the z direction. Consequently, this affects the excess pore air and water pressures. The physical implications of this mechanical process are captured in Equations (10) through (12) through the associated gravity parameter Π .

Assuming the top and bottom surfaces are permeable with respect to fluid flow, the appropriate boundary conditions are given by

$$p_1(h,t) = p_2(h,t) = 0, (13)$$

$$\left. \frac{\partial w}{\partial z} \right|_{(h,t)} = \frac{q(t)}{K_b + \frac{4}{3}G} \tag{14}$$

at z = h; and

$$p_1(0,t) = p_2(0,t) = 0, (15)$$

$$(K_b + \frac{4}{3}G)\frac{\partial w}{\partial z}\Big|_{(0,t)} = q(t) + \int_0^h (\Theta_s \frac{\partial w}{\partial z} + \Theta_1 p_1 + \Theta_2 p_2) dz$$
 (16)

at z=0. Figure 1(a) shows the schematic problem geometry and boundary conditions for this study. To examine the effect of body force and cyclic surface cyclic load q(t) on the poroelastic response of unsaturated soils, a triangular waveform for the cyclic load is chosen in what follows. The mathematical expression for q(t) is given by the infinite series

$$q(t) = -p^* \left\{ \frac{1}{2} + \sum_{i=1}^{\infty} \frac{2}{i^2 \pi^2} \left[1 - \cos(i\pi) \right] \cos(i\omega t) \right\},\tag{17}$$

where p^* is the stress amplitude, ω is the frequency of the cyclic load, and the negative sign implies that the load is compressive. Figure 1(b) shows a graphical representation of Equation (17) for $\omega = 0.1$ Hz and $p^* = 0.1$ MPa.

4 Numerical discretization

We use the finite difference scheme [21] in space and time to numerically solve the problem described in Section 3. For the spatial discretization, the secondorder symmetric finite difference in space and the first-order finite difference scheme in time are used. Selecting a uniform grid spacing of Δz and a time increment of Δt , the partial differential equations reduce to a system of linear equations of the form

$$(d_{1}-1)\frac{w'\frac{n+1}{k}-w'\frac{n}{k}}{\Delta t}+d_{2}\frac{p_{1}\frac{n+1}{k}-p_{1}\frac{n}{k}}{\Delta t}+d_{3}\frac{p_{2}\frac{n+1}{k}-p_{2}\frac{n}{k}}{\Delta t}$$

$$=\frac{\theta_{1}}{R_{11}}\Big[\frac{p_{1}\frac{n+1}{k+1}-2p_{1}\frac{n+1}{k}+p_{1}\frac{n+1}{k-1}}{\Delta z^{2}}-\rho_{1}d_{1}g\frac{w'\frac{n+1}{k+1}-w'\frac{n+1}{k-1}}{2\Delta z}$$

$$-\rho_{1}d_{2}g\frac{p_{1}\frac{n+1}{k+1}-p_{1}\frac{n+1}{k-1}}{2\Delta z}-\rho_{1}d_{3}g\frac{p_{2}\frac{n+1}{k+1}-p_{2}\frac{n+1}{k-1}}{2\Delta z}\Big], \quad (18)$$

$$(d_{4}-1)\frac{w'\frac{n+1}{k}-w'\frac{n}{k}}{\Delta t}+d_{5}\frac{p_{1}\frac{n+1}{k}-p_{1}\frac{n}{k}}{\Delta t}+d_{6}\frac{p_{2}\frac{n+1}{k}-p_{2}\frac{n}{k}}{\Delta t}$$

$$=\frac{\theta_{2}}{R_{22}}\Big[\frac{p_{2}\frac{n+1}{k+1}-2p_{2}\frac{n+1}{k}+p_{2}\frac{n+1}{k-1}}{\Delta z^{2}}-\rho_{2}d_{4}g\frac{w'\frac{n+1}{k+1}-w'\frac{n+1}{k-1}}{2\Delta z}$$

$$-\rho_{2}d_{5}g\frac{p_{1}\frac{n+1}{k+1}-p_{1}\frac{n+1}{k-1}}{2\Delta z}-\rho_{2}d_{6}g\frac{p_{2}\frac{n+1}{k+1}-p_{2}\frac{n+1}{k-1}}{2\Delta z}\Big], \quad (19)$$

and

$$\left(K_{b} + \frac{4}{3}G\right) \frac{w'_{k+1}^{n+1} - 2w'_{k}^{n+1} + w'_{k-1}^{n+1}}{\Delta z^{2}} - \alpha S_{1} \frac{p_{1}_{k+1}^{n+1} - 2p_{1}_{k}^{n+1} + p_{1}_{k-1}^{n+1}}{\Delta z^{2}} - \alpha S_{2} \frac{p_{2}_{k+1}^{n+1} - 2p_{2}_{k}^{n+1} + p_{2}_{k-1}^{n+1}}{\Delta z^{2}} + \Theta_{s} \frac{w'_{k+1}^{n+1} - w'_{k-1}^{n+1}}{2\Delta z} + \Theta_{1} \frac{p_{1}_{k+1}^{n+1} - p_{1}_{k-1}^{n+1}}{2\Delta z} + \Theta_{2} \frac{p_{2}_{k+1}^{n+1} - p_{2}_{k-1}^{n+1}}{2\Delta z} = 0, \quad (20)$$

where $p_{\xi_k}^n$ and w'_k^n $(k=1,2,\ldots,k_T)$ and $n=0,1,\ldots,n_T$ are the values of p_{ξ} and $w'\equiv \partial w/\partial z$ at the grid point k and time step n, respectively. The subscripts k=1 and $k=k_T$ are the bottom and top boundaries of the soil sample, respectively, i.e. $k_T=h/\Delta z+1$, whereas the superscripts n=0 and $n=n_T$ denote the initial and final time steps, respectively.

Similarly, we can recast the initial conditions in Section 3 as a discretization of the algebraic equations:

$$w_{k}^{0} = \frac{q^{0}}{K_{v}^{(u)}} \exp\left\{\frac{\Pi}{K_{v}^{(u)}} [h - (k-1)\,\Delta z]\right\},\tag{21}$$

$$p_{1k}^{0} = -\gamma_1 q^0 \exp\left\{\frac{II}{K_{*}^{(u)}} [h - (k-1)\Delta z]\right\},$$
 (22)

and

$$p_{2k}^{0} = -\gamma_2 q^0 \exp\left\{\frac{\Pi}{K_v^{(u)}} [h - (k-1)\Delta z]\right\}.$$
 (23)

The boundary conditions in Section 3 can also be represented in the following discretized form. At z = h,

$$p_{1k_{T}}^{n+1} = p_{2k_{T}}^{n+1} = 0 (24)$$

and

$$w'_{k_T}^{n+1} = \frac{q^{n+1}}{K_b + \frac{4}{3}G}.$$
 (25)

At z=0,

$$p_{11}^{n+1} = p_{21}^{n+1} = 0 (26)$$

and

$$\left(K_b + \frac{4}{3}G\right)w_1^{n+1} = q^{n+1} + \Theta_s\left(\frac{w_1^{n+1}}{2}\Delta z + \sum_{i=2}^{k_T-1} w_i^{n+1}\Delta z + \frac{w_{k_T}^{n+1}}{2}\Delta z\right)
+ \Theta_1\left(\frac{p_{1_1}^{n+1}}{2}\Delta z + \sum_{i=2}^{k_T-1} p_{1_i}^{n+1}\Delta z + \frac{p_{1_{k_T}}^{n+1}}{2}\Delta z\right)
+ \Theta_2\left(\frac{p_{2_1}^{n+1}}{2}\Delta z + \sum_{i=2}^{k_T-1} p_{2_i}^{n+1}\Delta z + \frac{p_{2_{k_T}}^{n+1}}{2}\Delta z\right).$$
(27)

As for the total settlement s(t), it can be evaluated in the following discretized form:

$$s(t) = -\int_0^h \frac{\partial w}{\partial z} dz = -\frac{1}{2} \left\{ \sum_{i=1}^{k_T - 1} w'_k^n \Delta z + \sum_{i=2}^{k_T} w'_k^n \Delta z \right\}.$$
 (28)

A system of linear equations can be developed after Equations (18) through (20) are imposed at each grid point and at each time step with the input of the initial and boundary conditions in Equations (21) through (23), and Equations (24) through (27). Employing the Gauss-Jordan elimination, we can then find the inverse of the coefficient matrix of the simultaneous system of equations, after which, the solution for excess pore water pressure and total settlement can be directly computed.

5 Numerical results and discussions

To implement the discretization scheme presented in Section 4, we need to evaluate the linear elasticity coefficients d_i $(i=1,\ldots,6)$ and relative mobilities $R_{\xi\xi}$ in Equations (1) through (3). Accordingly, the information about the water retention curve describing the relationship between the capillary pressure $p_c = p_1 - p_2$ and the water saturation S_2 , as well as the information about the relationship between the relative permeabilities $k_{r\xi}$ and the water saturation S_2 are required. The widely-applied van Genuchten-Mualem model [36, 42] was employed to quantify these relationships:

$$S_2^e = \frac{\theta_2 - \theta_2^r}{\theta_2^s - \theta_2^r} = [1 + (\chi h_c)^n]^{-m}, \tag{29}$$

$$k_{r1}(S_2^e) = (1 - S_2^e)^{\Lambda} [1 - (S_2^e)^{\frac{1}{m}}]^{2m},$$
 (30)

$$k_{r2}(S_2^e) = (S_2^e)^{\Lambda} \{1 - [1 - (S_2^e)^{\frac{1}{m}}]^m\}^2,$$
 (31)

where $h_c = p_c/\rho_2 g$ is the matric potential; χ , n, and m are model parameters obtained by fitting experimental data (m = 1 - 1/n); Λ is the pore connectivity parameter; and θ_2^r and θ_2^s are the residual and saturated volume fractions of

water, respectively [42]. We set the water saturation S_2 equal to the effective water saturation S_2^e in Equations (29) through (31). We note that the water retention curve and relative permeability function are dynamic, saturation-dependent processes. However, when addressing the behavior of an elastic porous medium undergoing small deformations within the theory of poroelasticity, these relationships are thus evaluated in a reference configuration, taken here as the unperturbed state prior to application of an external load.

In this section, we present a series of numerical examples demonstrating the impact of gravity on the solid-fluid interaction in homogeneous, isotropic unsaturated soils. For the first example, we study the consolidation problem without gravitational compaction, which reduces to the benchmark model for the generalization of Biot theory to a two-fluid system [35] that provides the analytical, closed-form solution for the excess pore water and air pressures together with the total settlement under time-dependent stress loading. Tables 1 and 2 list the elasticity and hydraulic parameters necessary for numerical calculation with the fitting coefficients for the water retention curve and hydraulic conductivity function. Figure 2 shows the comparison between the numerical and analytical solutions for the distribution of the dimensionless pore water pressure (p_2/p^*) with respect to the dimensionless depth (z/h)in an unsaturated clayed soil for $S_2 = 0.7$ and $S_2 = 0.9$ at $\omega = 0.1$ Hz and h = 10 m, respectively. The temporal evolution of the corresponding total settlement with elapse time is graphically depicted in Figure 3. In the current study, the finite difference framework is carried out in Fortran with a time step $\Delta t = 1$ sec and a spatial increment of $\Delta z = 0.05$ m. Based on Figures 2 and 3, it is evident that an excellent agreement is demonstrated between the two solutions, indicating the stability and accuracy of the proposed finite difference scheme.

Next, we examine the impact of gravity forces on the development of excess pore water pressure at different depths of unsaturated soils. Figure 4 shows the relationship between the dimensionless pore water pressure and elapsed time at the individual dimensionless depths of 0.25, 0.5, and 0.75 in an unsaturated clayey soil (h = 10 m), with $S_2 = 0.7$ and subjected to an excitation frequency of $\omega = 0.1$ Hz. The corresponding relative difference is also given, which is calculated as the difference between the dimensionless pore water pressure computed with and without gravitational compaction and normalized with respect to the pressure without gravitational compaction. The relationship is also investigated with a higher saturation $S_2 = 0.9$ in Figure 5. It can be seen from Figures 4 and 5 that the relative difference caused by gravitational compaction decreases with a decrease in the soil thickness but with an increase in water saturation. One possible physical cause behind the observed result may be that soils with less saturation levels under a gravity field offer greater resistance to cyclic loading compared to those with more saturation levels. Apart from the changes in the pore water pressure, we can also gain a detailed insight into how gravity forces affect the total settlement, which is portrayed in Figure 6 for $S_2 = 0.7$ and $S_2 = 0.9$. The increase of settlement shown in Figure 6 confirms the observations from Figures 4 and 5. Quantitatively, there is a relative difference in the total settlement owing to the inclusion of gravity effect of around 1% for this example. As an aside, we note that the discontinuity occurs in these plots because the denominator (total settlement without gravitational compaction) approaches zero, leading to a singularity. Accordingly, with the numerical analyses in the present paper and our previous study [14, 30], an important inference is that regardless of whether external stress loads are constant or time-variant, gravity forces have a more significant impact on unsaturated soils than on saturated soils.

The excitation frequency is the key feature governing the general mechanical behavior of water-permeated soils under the action of cyclic loading. Its influence on the dependence of the dimensionless pore water pressure on elapse time and depth is illustrated in Figures 7 and 8 with small excitation frequency (ω =0.001 Hz) for lower ($S_2 = 0.7$) and higher ($S_2 = 0.9$) water saturations, respectively. Inspection of Figures 4 and 5 as well as Figures 7 and 8 reveals that the excitation frequency appears not to render an obvious impact on the pore water pressure as gravitational body forces are taken into account in the model of poroelasticity. This remark is also true for the total settlement by examining Figures 6 and 9. To show the complete cyclic response of the excess pore water pressure to two different frequencies of 0.1Hz and 0.001Hz, distinctive time scales are used in Figures 4-5 (second) and Figures 7-8 (minute), respectively. It is also noted that these two excitation frequencies fall within the range that ensures the consolidation problem of poroelasticity to remain sufficiently accurate in a quasi-static analysis so that second-order time-derivative terms can be neglected in Equations (1) through (3) [35].

Next, we are concerned with whether the length of the soil sample is of great importance in characterizing changes in the dimensionless pore water pressure caused by gravity forces. This physical behavior is studied in Figures 10 and 11 for a longer soil sample (h=100 m) with S_2 = 0.7 and S_2 = 0.9 under ω =0.001 Hz, respectively. A logical inference from comparison of Figures 7 and 8 as well as Figures 10 and 11 indicates that the effect of gravitational compaction becomes more significant for pore water pressure as the soil sample has more length. This can be radically understood that the longer the soil sample, the more its weight, leading to more gravitational compaction. This conclusion is also consistent with the result as revealed in Figures 9 and 12 for variations in the total settlement brought about by gravitational compaction. The relative difference turns out to be very significant, heightened from 1% to 10% as h is altered from 10 m to 100 m.

Soil compressibility is one of the dominant material properties in response to mechanical loads. Figures 13 and 14 provide numerical results for the dimensionless pore water pressure as function of the dimensionless depth (z/h) in a more stiffer soil, sand, with $S_2=0.7$ and $S_2=0.9$ ($h{=}100$ m, $\omega{=}0.001$ Hz), respectively. By contrast to clayed soil, smaller relative difference occurs in sandy soil. The same observation is also confirmed for the total settlement

in Figure 15. A straightforward conclusion can be drawn that gravitational compaction has more substantial influence in more compressible soils.

6 Conclusions

Gravitational compaction results in increased material density and alters the volumetric fraction of all constituents in variably-saturated porous materials. It is commonly neglected in the theory of poroelasticity partly because it makes the governing equations more complicated, thereby inhibiting the formulation of an analytical, closed form solution. In this paper, we consider the effects of gravitational compaction for unsaturated soils subjected to cyclic loading. Our mathematical model is based on the generalized theory of poroelasticity for a two-fluid system [30] accounting for the gravitational body forces. We formulate the solution for a soil deposit subjected to cyclic surface load with a triangle-waveform. In one-dimensional representation, this requires the introduction of an additional variable into the formulation, namely, the gradient of the vertical displacement, $\partial w/\partial z$, in addition to the pore air and water pressures.

Our solution is based on a load-prescribed boundary-value problem in which the unsaturated soil deposit is subjected to fully permeable boundary conditions at both the top and bottom ends. Under a harmonic stress load on the top surface, the displacement variation is no longer monotonic, but instead becomes a time-dependent function. A numerical algorithm based on the finite difference scheme is thus carried out. The results in this paper highlight for the first time that gravitational compaction has a negative correlation with water saturation (i.e., the higher the saturation, the smaller the effect of gravitational compaction). However, the effect of gravitational compaction becomes more significant with an increase in the height of the soil column, with the increase varying linearly with this height. Therefore, gravitational body forces should be incorporated into the model of poroelasticity for deeper soil deposits. Lastly, we show that soil compressibility enhances the effect of gravitational compactions, which is shown to increase with the compressibility of the soil.

A Representation of the poroelasticity coefficients d_i

Following Lo et al. [28], the poroelasticity coefficients d_i for i = 1, ..., 6 can be expressed in terms of the volumetric fraction θ_{ξ} of fluid phase ξ and the elasticity coefficients a_{ij} (for i, j = 1, 2, 3) defined in Lo et al. [23]:

$$d_1 = \frac{a_{12}a_{33} - a_{13}a_{23}}{a_{23}^2 - a_{22}a_{33}},\tag{A1}$$

Modeling pore fluid pressure and deformation in unsaturated soils

$$d_2 = \frac{\theta_1 a_{33}}{a_{23}^2 - a_{22} a_{33}},\tag{A2}$$

13

$$d_3 = -\frac{\theta_2 a_{23}}{a_{23}^2 - a_{22} a_{33}},\tag{A3}$$

$$d_4 = \frac{a_{13}a_{22} - a_{12}a_{23}}{a_{23}^2 - a_{22}a_{33}},\tag{A4}$$

$$d_5 = -\frac{\theta_1 a_{23}}{a_{23}^2 - a_{22} a_{33}},\tag{A5}$$

$$d_6 = \frac{\theta_2 a_{22}}{a_{23}^2 - a_{22} a_{33}}. (A6)$$

In view of Lo et al. [23], a_{ij} can be modeled by directly-measurable parameters:

$$a_{11} = K_s(1 - \phi - \delta_s), \tag{A7}$$

$$a_{12} = -K_s \delta_1, \tag{A8}$$

$$a_{13} = -K_s \delta_2, \tag{A9}$$

$$a_{22} = -\frac{1}{M_1} [(K_1 K_2 \frac{dS_1}{dp_c} + \frac{K_1 K_2 S_1}{1 - S_1} \frac{dS_1}{dp_c} + K_1 S_1) \delta_1 + \frac{K_1 K_2 S_1 \phi}{1 - S_1} \frac{dS_1}{dp_c} + K_1 S_1 \phi],$$
(A10)

$$a_{23} = -\left(\frac{\delta_1 \delta_2}{\delta_s} K_s + \frac{K_1 K_2 \phi}{M_1} \frac{dS_1}{dp_c}\right), \tag{A11}$$

$$a_{33} = -\frac{1}{M_1} \{ [K_1 K_2 \frac{dS_1}{dp_c} + \frac{K_1 K_2 (1 - S_1)}{S_1} \frac{dS_1}{dp_c} + K_2 (1 - S_1)] \delta_2 + \frac{K_1 K_2 (1 - S_1) \phi}{S_1} \frac{dS_1}{dp_c} + K_2 (1 - S_1) \phi \},$$
(A12)

where K_1 and K_2 denote the bulk moduli of the air and water phases, respectively. In Equations (A7) through (A12), δ_s , δ_1 , and δ_2 are dimensionless parameters defined to specify the closure equation for porosity change; while M_1 and M_2 are two effective non-wetting fluid storativity factors associated with the capillary pressure curve:

$$\delta_s = \frac{(1 - \phi - \frac{K_b}{K_s})K_s}{K_s + \frac{M_2}{M_s}(\frac{K_b}{K_s} - 1 + \phi)},\tag{A13}$$

$$\delta_1 = \frac{K_1(S_1 + K_2 \frac{dS_1}{dp_c} + \frac{K_2 S_1}{1 - S_1} \frac{dS_1}{dp_c})(1 - \phi - \frac{K_b}{K_s})}{K_s M_1 + M_2(\frac{K_b}{K_s} - 1 + \phi)},$$
(A14)

$$\delta_2 = \frac{K_2(1 - S_1 + \frac{K_1}{S_1} \frac{dS_1}{dp_c})(1 - \phi - \frac{K_b}{K_s})}{K_s M_1 + M_2(\frac{K_b}{K_c} - 1 + \phi)},$$
(A15)

$$M_1 = -\left(\frac{K_1}{S_1} \frac{dS_1}{dp_c} + \frac{K_2}{1 - S_1} \frac{dS_1}{dp_c} + 1\right),\tag{A16}$$

$$M_2 = \frac{K_1 K_2}{\phi S_1 (1 - S_1)} \frac{dS_1}{dp_c} + \frac{K_1 S_1}{\phi} + \frac{K_2 (1 - S_1)}{\phi}.$$
 (A17)

Acknowledgments

The first author is grateful for the support received from the National Science and Technology Council, Taiwan, under Contract no. 112-2917-I-564-004. The second author is supported by the U.S. National Science Foundation under Award Number CMMI-1914780. Gratitude is expressed by the third author for financial support by National Cheng Kung University through the National Science and Technology Council, Taiwan under Contract no. 112-2625-M-006-019.

References

- [1] Biot, M.A., 1941. General theory of three-dimensional consolidation. J. Appl. Phys., 12(2), 155–164.
- [2] Biot, M.A., 1956. Theory of propagation of elastic waves in a fluid-saturated porous solid. I. Low-frequency range, II. Higher frequency range. J. Acoust. Soc. 28(2), 168–191.
- [3] Biot, M.A., Willis, D.G., 1957. The elastic coefficients of the theory of consolidation. J. Appl. Mech. 24, 594–601.
- [4] Biot, M.A., 1962. Mechanics of deformation and acoustic propagation in porous media. J. Appl. Phys. 33(4), 1482–1498.
- [5] Borja, R.I., 2004. Cam-Clay plasticity. Part V: A mathematical framework for three-phase deformation and strain localization analyses of partially saturated porous media. Comput. Methods Appl. Mech. Eng. 193(48–51), 5301–5338.
- [6] Borja, R.I., 2006. On the mechanical energy and effective stress in saturated and unsaturated porous continua. Int. J. Solids Struct. 43(6), 1764–1786.
- [7] Borja, R.I., Koliji, A., 2009. On the effective stress in unsaturated porous continua with double porosity. J. Mech. Phys. Solids 57(8), 1182–1193.

- [8] Borja, R.I., White, J.A., 2010. Continuum deformation and stability analyses of a steep hillside slope under rainfall infiltration. Acta Geotech. 5, 1–14.
- [9] Borja, R.I., Liu, X., White, J.A., 2012. Multiphysics hillslope processes triggering landslides. Acta Geotech. 7, 261–269.
- [10] Borja, R.I., White, J.A., Liu, X., Wu, W., 2012. Factor of safety in a partially saturated slope inferred from hydro-mechanical continuum modeling. Int. J. Numer. Anal. Methods Geomech. 36(2), 236–248.
- [11] Borja, R.I., Song, X., Wu, W., 2013. Critical state plasticity. Part VII: Triggering a shear band in variably saturated porous media. Comput. Methods Appl. Mech. Eng. 261, 66–82.
- [12] Casciati, S., Borja, R.I., 2004. Dynamic FE analysis of South Memnon Colossus including 3D soil–foundation–structure interaction. Comput. Struct. 82(20-21), 1719–1736.
- [13] Causon, D.M., Mingham, C.G., 2010. Introductory Finite Difference Methods for PDEs. BookBoon.
- [14] Chao, N.C., Lee, J.W., Lo, W.C., 2018. Gravity effect on consolidation in poroelastic soils under saturated and unsaturated conditions. J. Hydrol. 566, 99–108.
- [15] Choo, J., White, J.A., Borja, R.I., 2016. Hydromechanical modeling of unsaturated flow in double porosity media. Int. J. Geomech. 16(6), D4016002.
- [16] Deng, J.H., Lee, J.W., Lo, W.C., 2019. Closed-form solutions for onedimensional consolidation in saturated soils under different waveforms of time-varying external loading. J. Hydrol. 573, 395–405.
- [17] Ding, P., Xu, R., Ju, L., Qiu, Z., Cheng, G., Zhan, X., 2021. Semi-analytical analysis of fractional derivative rheological consolidation considering the effect of self-weight stress. Int. J. Numer. Anal. Methods Geomech. 45, 1049–1066.
- [18] Ebel, B.A., Loague, K., Borja, R.I., 2010. The impacts of hysteresis on variably saturated hydrologic response and slope failure. Environ. Earth Sci. 61, 1215–1225.
- [19] Feng, J., Ni, P., Mei, G., 2019. One-dimensional self-weight consolidation with continuous drainage boundary conditions: Solution and application to clay-drain reclamation. Int. J. Numer. Anal. Methods Geomech. 43, 1634–1652.
- [20] Gibson, R.E., Schiffman, R.L., Cargill, K.W., 1981. The theory of onedimensional consolidation of saturated clays. II. Finite nonlinear consolidation of thick homogeneous layers, Can. Geotech. J. 18, 280–293.
- [21] Langtangen, H.P., Linge, S., 2017. Finite difference computing with PDEs: a modern software approach. Springer Nature.
- [22] Lo, W.C., Sposito, G., Majer, E., 2002. Immiscible two-phase fluid flows in deformable porous media. Adv. Water Resour. 25(8-12), 1105–1117.

- [23] Lo, W.C., Sposito, G., Majer, E., 2005. Wave propagation through elastic porous media containing two immiscible fluids. Water Resour. Res. 41(2).
- [24] Lo, W.C., Yeh, C.L., Tsai, C.T., 2007. Effect of soil texture on the propagation and attenuation of acoustic wave at unsaturated conditions. J. Hydrol. 338(3-4), 273–284.
- [25] Lo, W.C., Sposito, G., Majer, E., 2009. Analytical decoupling of poroelasticity equations for acoustic-wave propagation and attenuation in a porous medium containing two immiscible fluids. J. Eng. Math. 64, 219– 235.
- [26] Lo, W.C., Sposito, G., Huang, Y.H., 2012. Modeling seismic stimulation: Enhanced non-aqueous fluid extraction from saturated porous media under pore-pressure pulsing at low frequencies. J. Appl. Geophys. 78, 77–84.
- [27] Lo, W.C., Sposito, G., 2013. Acoustic waves in unsaturated soils. Water Resour. Res. 49(9), 5674–5684.
- [28] Lo, W.C., Sposito, G., Chu, H., 2014. Poroelastic theory of consolidation in unsaturated soils. Vadose Zone J. 13(5), 1–12.
- [29] Lo, W.C., Sposito, G., Lee, J.W., Chu, H. 2016. One-dimensional consolidation in unsaturated soils under cyclic loading. Adv. Water Resour. 91, 122–137.
- [30] Lo, W.C., Chao, N.C., Chen, C.H., Lee, J.W., 2017. Poroelastic theory of consolidation in unsaturated soils incorporating gravitational body forces. Adv. Water Resour. 106, 121–131.
- [31] Lo, W.C., Borja, R.I., Deng, J.H., Lee, J.W., 2020. Analytical solution of soil deformation and fluid pressure change for a two-layer system with an upper unsaturated soil and a lower saturated soil under external loading. J. Hydrol. 588, 124997.
- [32] Lo, W.C., Borja, R.I., Deng, J.H., Lee, J.W., 2021. Poroelastic theory of consolidation for a two-layer system with an upper unsaturated soil and a lower saturated soil under fully permeable boundary conditions. J. Hydrol. 596, 125700.
- [33] Lo, W.C., Chang, J.C., Borja, R.I., Deng, J.H., Lee, J.W., 2021. Mathematical modeling of consolidation in unsaturated poroelastic soils under fluid flux boundary conditions. J. Hydrol. 595, 125671.
- [34] Lo, W.C., Purnomo, S.N., Dewanto, B.G., Sarah, D., Sumiyanto, 2022. Integration of numerical models and InSAR techniques to assess land subsidence due to excessive groundwater abstraction in the coastal and lowland regions of Semarang city. Water 14(2), 201.
- [35] Lo, W.C., Borja, R.I., Chao, N.C., Liu, Y.C., Lee, J.W., 2024. Poroelastic response of unsaturated soils to cyclic loads with arbitrary waveforms. Int. J. Numer. Anal. Methods Geomech. 48(3), 679-700.
- [36] Mualem, Y., 1976. A new model for predicting the hydraulic conductivity of unsaturated porous media. Water Resour. Res. 12(3), 513–522.

- [37] Rawls, W.J., Ahuja, L.R., Brakensiek, D.L., 1992. Estimating soil hydraulic properties from soils data. In Indirect methods for estimating the hydraulic properties of unsaturated soils, 32(9), 329–340.
- [38] Song, X., Borja, R.I., 2014. Mathematical framework for unsaturated flow in the finite deformation range. Int. J. Numer. Methods Eng. 97(9), 658–682.
- [39] Song, X., Borja, R.I., 2014. Finite deformation and fluid flow in unsaturated soils with random heterogeneity. Vadose Zone J. 13(5), 1–11.
- [40] Truesdell, C., 1984. Historical introit the origins of rational thermodynamics. Springer.
- [41] Uzuoka, R., Borja, R.I., 2012. Dynamics of unsaturated poroelastic solids at finite strain. Int. J. Numer. Anal. Methods Geomech. 36(13), 1535–1573.
- [42] van Genuchten, M.T., 1980. A closed-form equation for predicting the hydraulic conductivity of unsaturated soils. Soil Sci. Soc. Am. J. 44(5), 892–898.
- [43] Wang, H., 2000. Theory of linear poroelasticity with applications to geomechanics and hydrogeology. Princeton University Press.
- [44] Xie, X., Zhang, J., Zeng, G., 2005. Similarity solution of self-weight consolidation problem for saturated soil. Appl. Math. Mech. 26, 1165– 1171.
- [45] Xu, C.T., Wang, Z.J., Xie, X.Y., Zheng, L.W., 2023. Analysis of the most efficient horizontal drainage position in the large strain consolidation considering the self-weight effect. Comput. Geotech. 154, 105106.
- [46] Zhang, Q., Borja, R.I., 2021. Poroelastic coefficients for anisotropic single and double porosity media. Acta Geotech. 16(10), 3013–3025.
- [47] Zhao, Y., Borja, R.I., 2020. A continuum framework for coupled solid deformation—fluid flow through anisotropic elastoplastic porous media. Comput. Methods Appl. Mech. Eng. 369,113225.
- [48] Zhao, Y., Borja, R.I., 2021. Anisotropic elastoplastic response of double-porosity media. Comput. Methods Appl. Mech. Eng. 380, 113797.
- [49] Zoback, M.D., 2010. Reservoir geomechanics. Cambridge University Press.

18 Chao et al.

Table 1. Material parameters for unsaturated clayed and sandy soils. After Rawls et al. [37] and Lo et al. [24].

Soil Textural Class	Clay	Sand
Porosity, ϕ	0.475	0.437
Fitting parameter, χ (1/m)	1.168	6.258
Fitting parameter, Λ	1.165	1.694
Intrinsic permeability, $k_s \times 10^{-14} \text{ (m}^2\text{)}$	1.7	595
Bulk modulus, K_b (MPa)	4.5	35.3
Shear modulus, G (MPa)	2.4	13.3

Table 2. Material parameters for unsaturated clayed and sandy soils after Rawls et al. [37] and Lo et al. [24]. Maximum applied stress $p^* = 0.1$ MPa.

Material Parameter	Value
Bulk modulus of soild, K_s (GPa)	35
Bulk modulus of air, K_1 (MPa)	0.145
Bulk modulus of water, K_2 (GPa)	2.25
Material density of water, ρ_2 (kg/m ³)	997
Viscosity of air, $\eta_1 \times 10^{-6} \text{ (Ns/m}^2\text{)}$	18
Viscosity of water, η_2 (Ns/m ²)	0.001

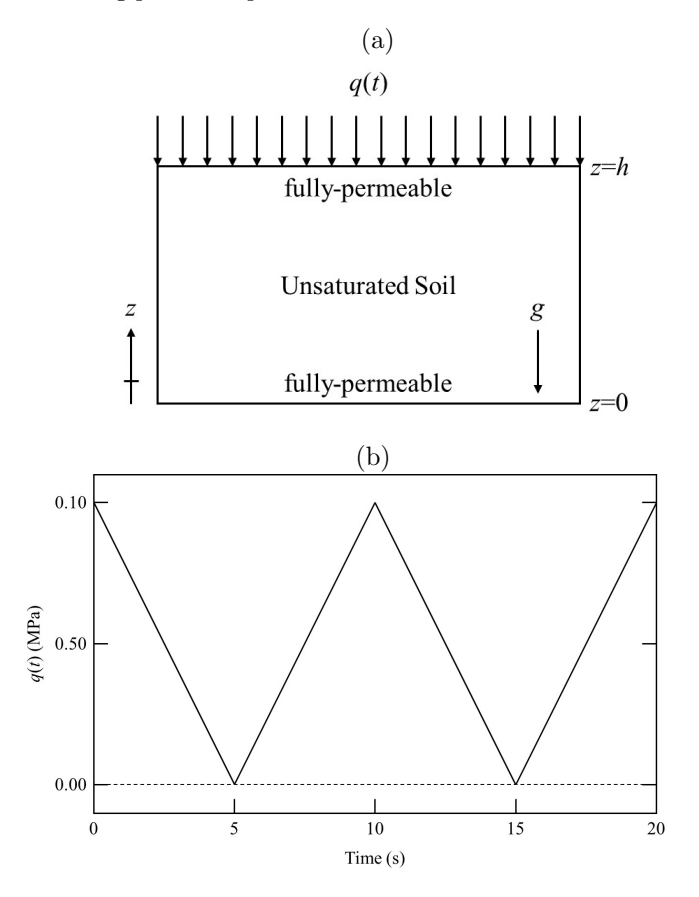


Fig. 1. (a) schematic diagram of the initial boundary-value problem, and (b) graphic representation of a triangular loading with excitation frequency $\omega=0.1$ Hz.

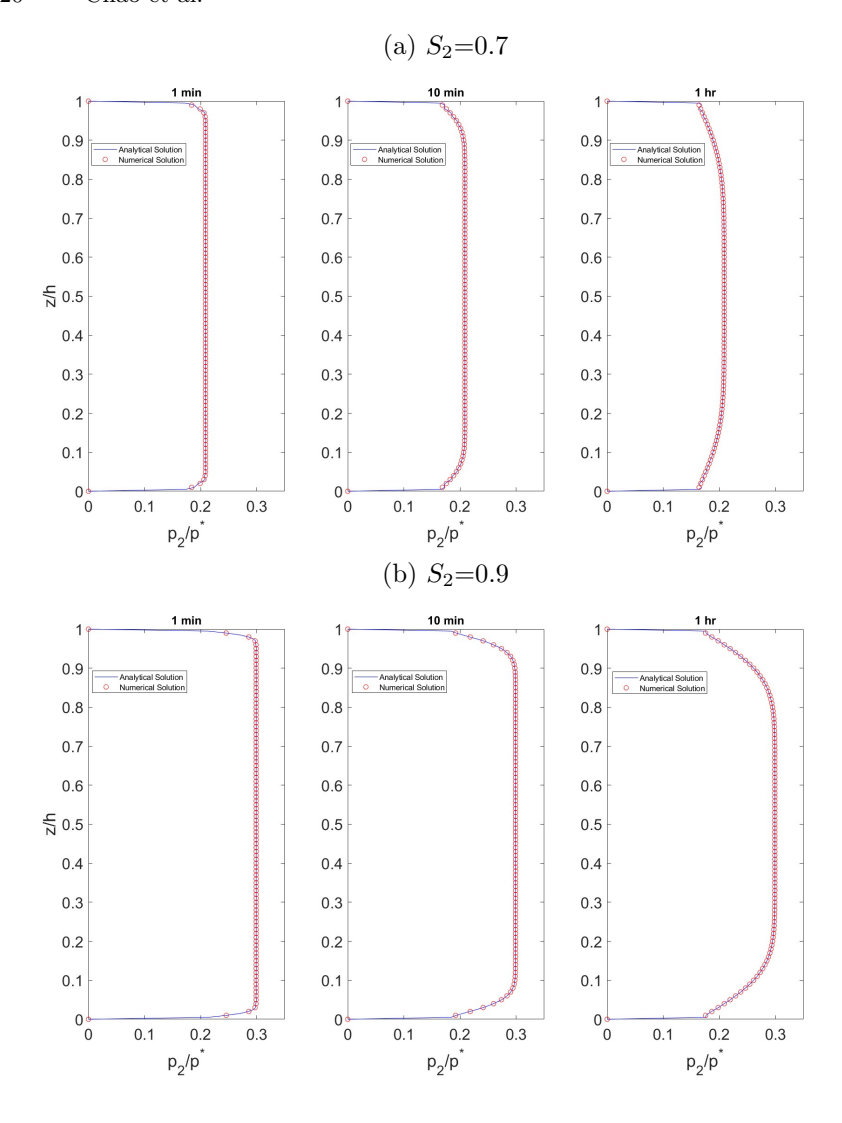
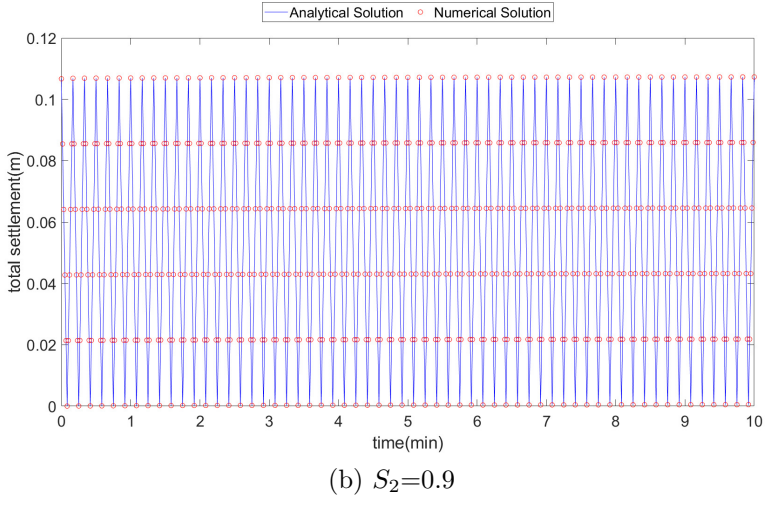


Fig. 2. Comparison of the results between the numerical and analytical solutions [35] for the distribution of the dimensionless pore water pressure (p_2/p^*) with respect to the dimensionless depth (z/h) in an unsaturated clayed soil $(h=10 \text{ m}, \omega=0.1 \text{ Hz})$ (a) $S_2=0.7$ and (b) $S_2=0.9$.





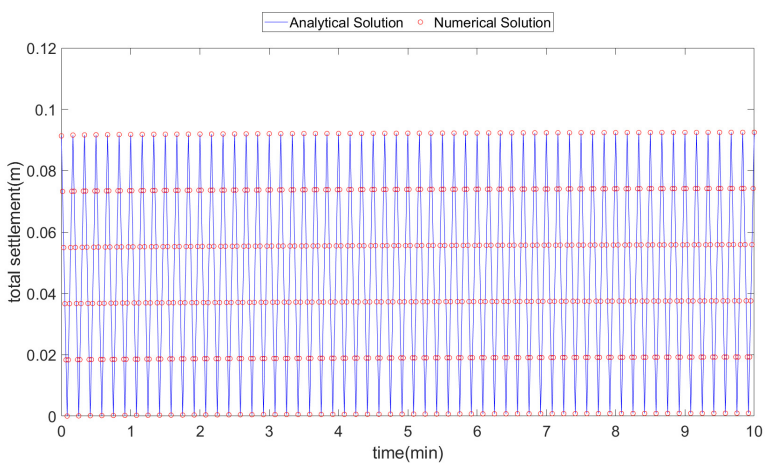


Fig. 3. Comparison of the results between the numerical and analytical solutions [35] for the evolution of the total settlement with elapse time in an unsaturated clayed soil (h=10 m, ω =0.1 Hz) (a) S_2 = 0.7 and (b) S_2 = 0.9.

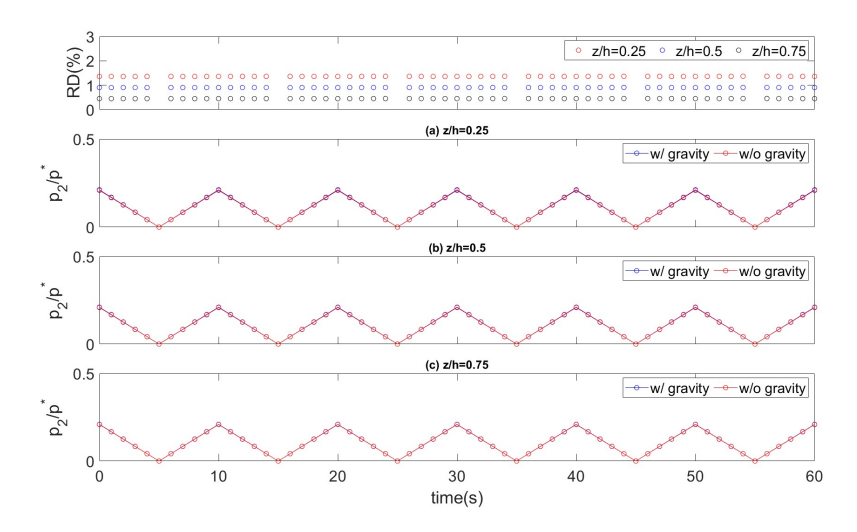


Fig. 4. Variations in the relationship between the dimensionless pore water pressure (p_2/p^*) and elapse time (t) at (a) z/h = 0.2, (b) z/h = 0.5, (c) z/h = 0.75 for an unsaturated clayed soil $(S_2 = 0.7, h = 10 \text{ m}, \omega = 0.1 \text{ Hz})$ due to gravity forces as well as the relative difference (RD).

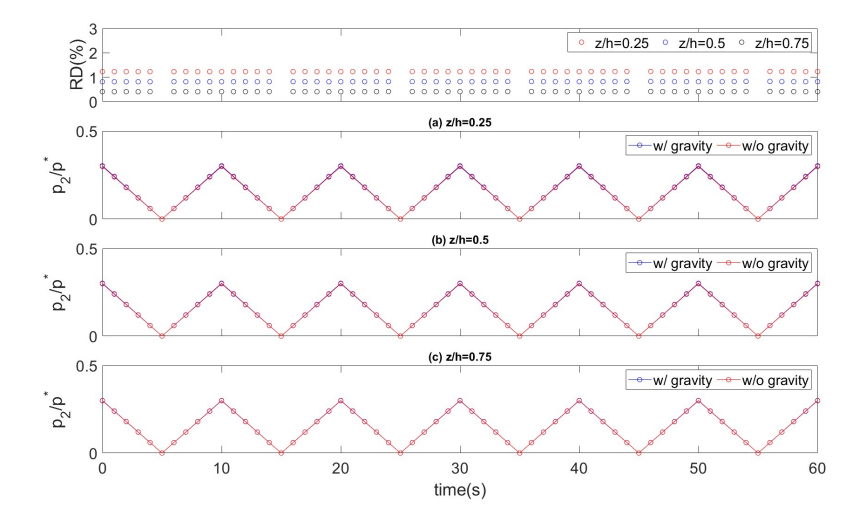


Fig. 5. Variations in the relationship between the dimensionless pore water pressure (p_2/p^*) and elapse time (t) at (a) z/h=0.25, (b) z/h=0.5, (c) z/h=0.75 for an unsaturated clayed soil $(S_2=0.9,\ h=10\ \mathrm{m},\ \omega=0.1\ \mathrm{Hz})$ due to gravity forces as well as the relative difference (RD).

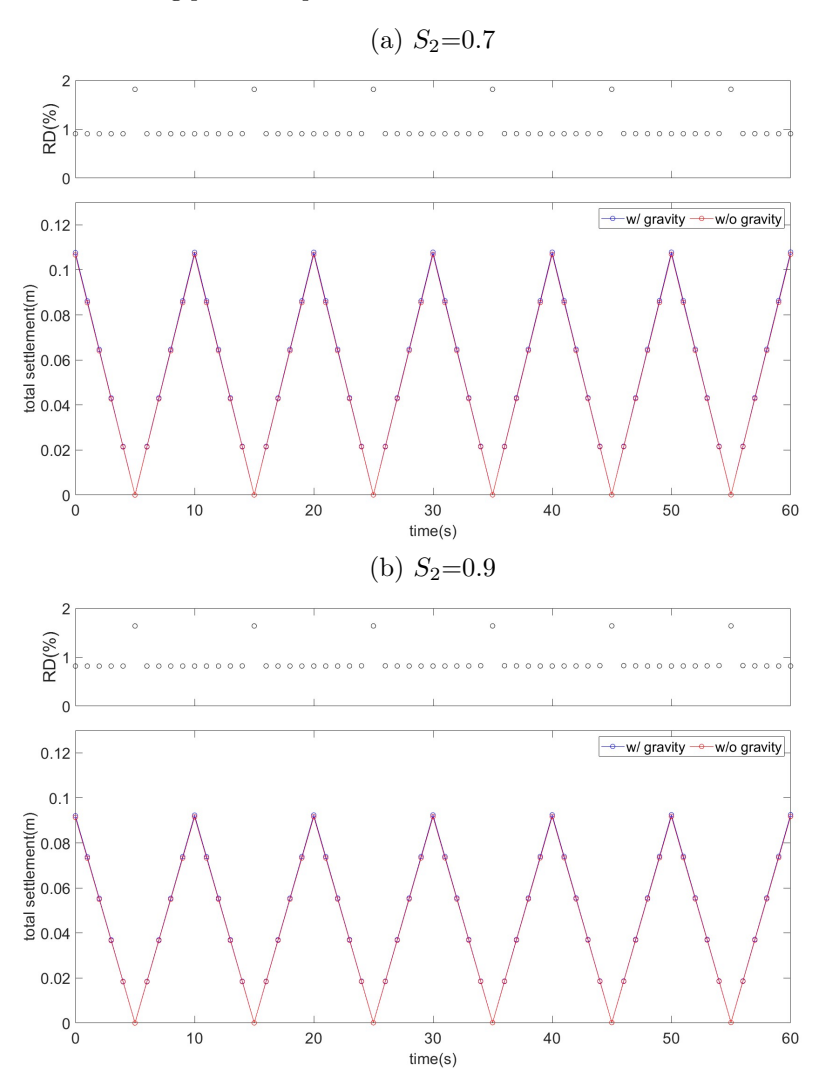


Fig. 6. Variations in the relationship between the total settlement and elapsed time (t) for an unsaturated clayed soil $(h=10 \text{ m}, \omega=0.1 \text{ Hz})$ for (a) $S_2=0.7$ and (b) $S_2=0.9$ due to gravity forces as well as the relative difference (RD).

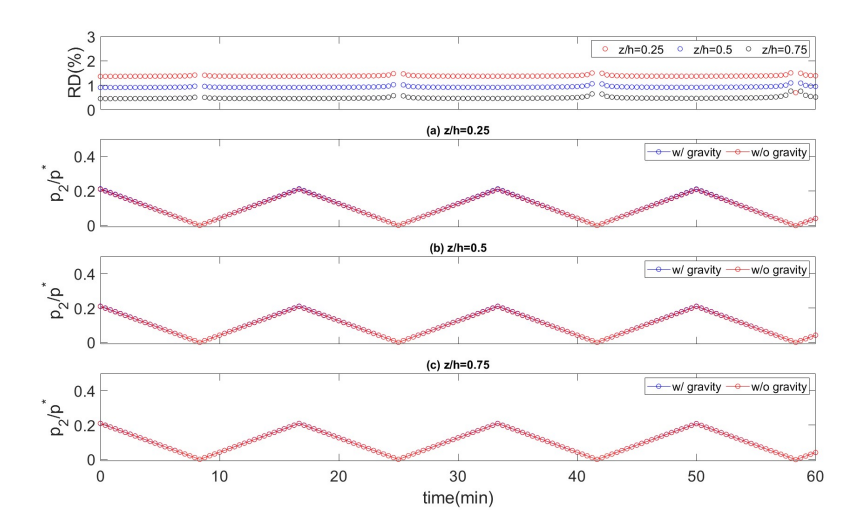


Fig. 7. Variations in the relationship between the dimensionless pore water pressure (p_2/p^*) and elapse time (t) at (a) z/h = 0.25, (b) z/h = 0.5, (c) z/h = 0.75 for an unsaturated clayed soil $(S_2 = 0.7, h = 10 \text{ m}, \omega = 0.001 \text{ Hz})$ due to gravity forces as well as the relative difference (RD).

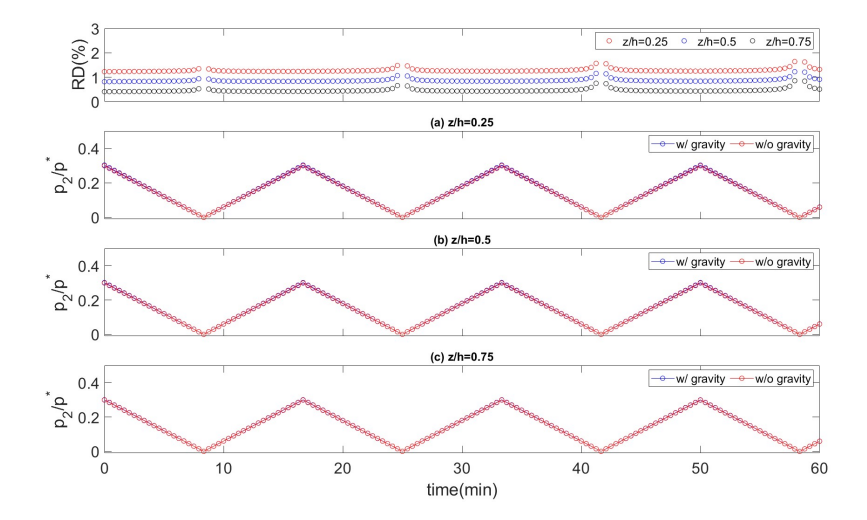


Fig. 8. Variations in the relationship between the dimensionless pore water pressure (p_2/p^*) and elapse time (t) at (a) z/h=0.25, (b) z/h=0.5, (c) z/h=0.75 for an unsaturated clayed soil ($S_2 = 0.9$, h=10 m, ω =0.001 Hz) due to gravity forces as well as the relative difference (RD).

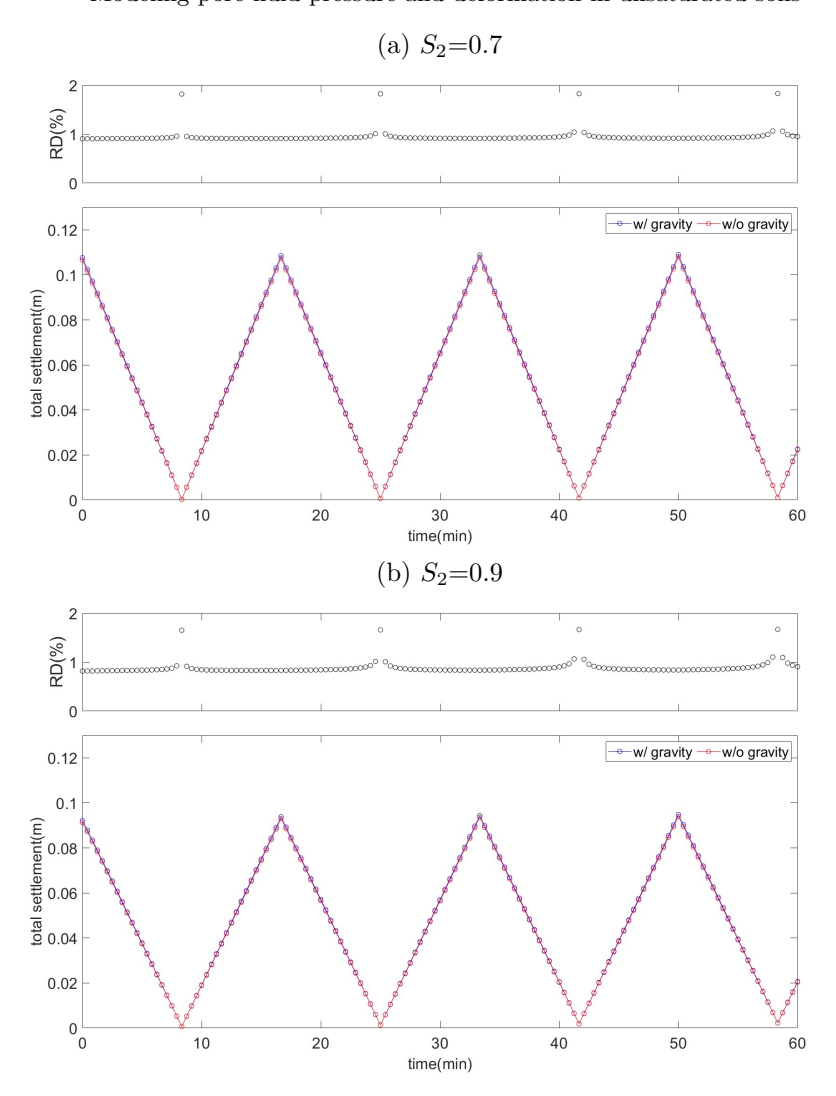


Fig. 9. Variations in the relationship between the total settlement and elapsed time (t) for an unsaturated clayed soil (h=10 m, $\omega=0.001$ Hz) for (a) $S_2=0.7$ and (b) $S_2=0.9$ due to gravity forces as well as the relative difference (RD).

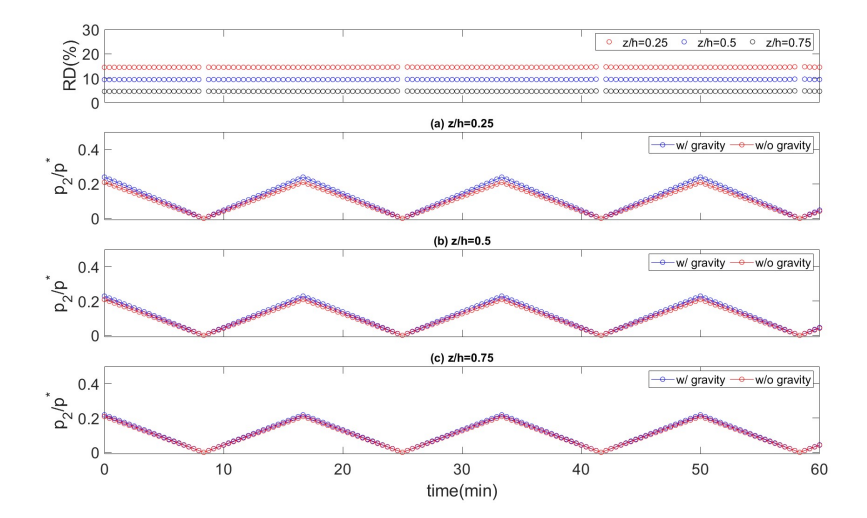


Fig. 10. Variations in the relationship between the dimensionless pore water pressure (p_2/p^*) and elapse time (t) at (a) z/h = 0.25, (b) z/h = 0.5, (c) z/h = 0.75 for an unsaturated clayed soil $(S_2 = 0.7, h = 100 \text{ m}, \omega = 0.001 \text{ Hz})$ due to gravity forces as well as the relative difference (RD).

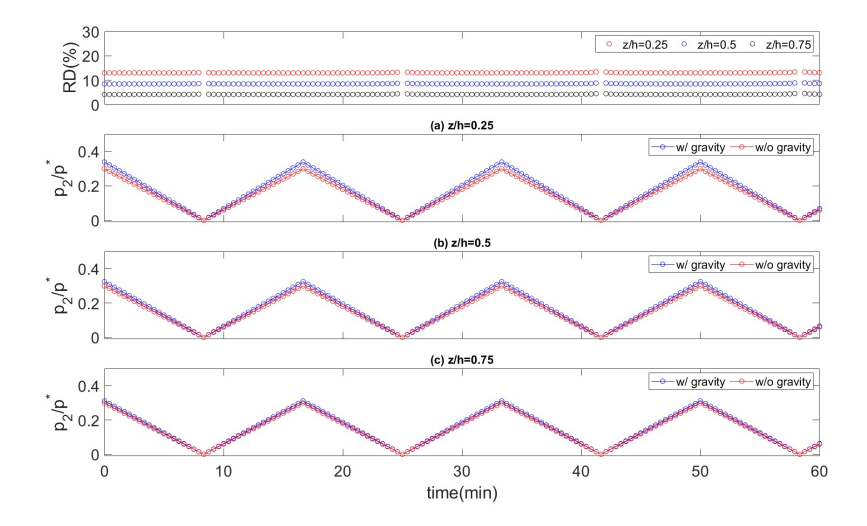


Fig. 11. Variations in the relationship between the dimensionless pore water pressure (p_2/p^*) and elapsed time (t) at (a) z/h = 0.25, (b) z/h = 0.5, (c) z/h = 0.75 for an unsaturated clayed soil $(S_2 = 0.9, h = 100 \text{ m}, \omega = 0.001 \text{ Hz})$ due to gravity forces as well as the relative difference (RD).

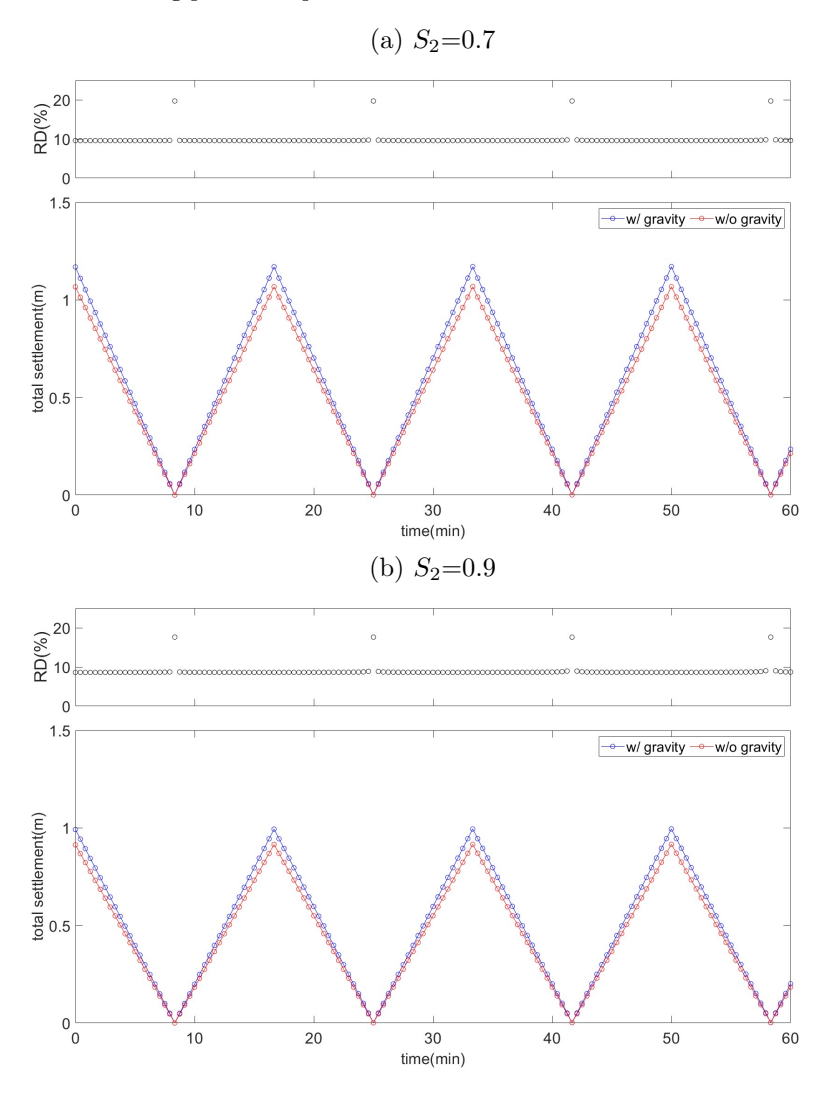


Fig. 12. Variations in the relationship between the total settlement and elapsed time (t) for an unsaturated clayed soil ($h=100~\mathrm{m},\,\omega=0.001~\mathrm{Hz}$) for (a) $S_2=0.7$ and (b) $S_2=0.9$ due to gravity forces as well as the relative difference (RD).

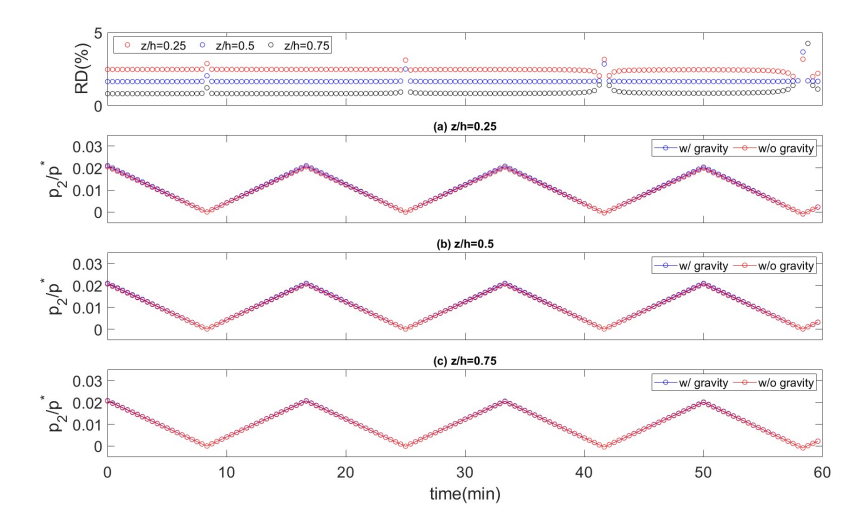


Fig. 13. Variations in the relationship between the dimensionless pore water pressure (p_2/p^*) and elapse time (t) at (a) z/h = 0.25, (b) z/h = 0.5, (c) z/h = 0.75 for an unsaturated sandy soil $(S_2 = 0.7, h = 100 \text{ m}, \omega = 0.001 \text{ Hz})$ due to gravity forces as well as the relative difference (RD).

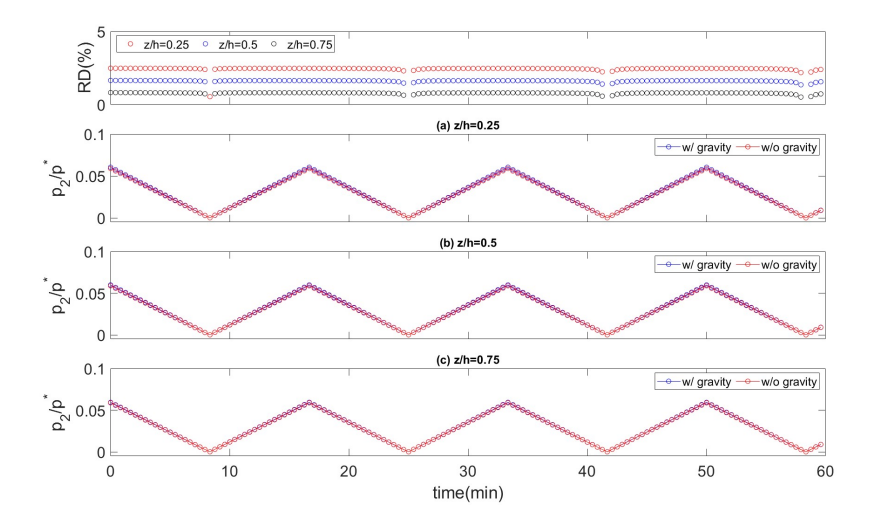


Fig. 14. Variations in the relationship between the dimensionless pore water pressure (p_2/p^*) and elapsed time (t) at (a) z/h = 0.25, (b) z/h = 0.5, (c) z/h = 0.75 for an unsaturated sandy soil $(S_2 = 0.9, h = 100 \text{ m}, \omega = 0.001 \text{ Hz})$ due to gravity forces as well as the relative difference (RD).

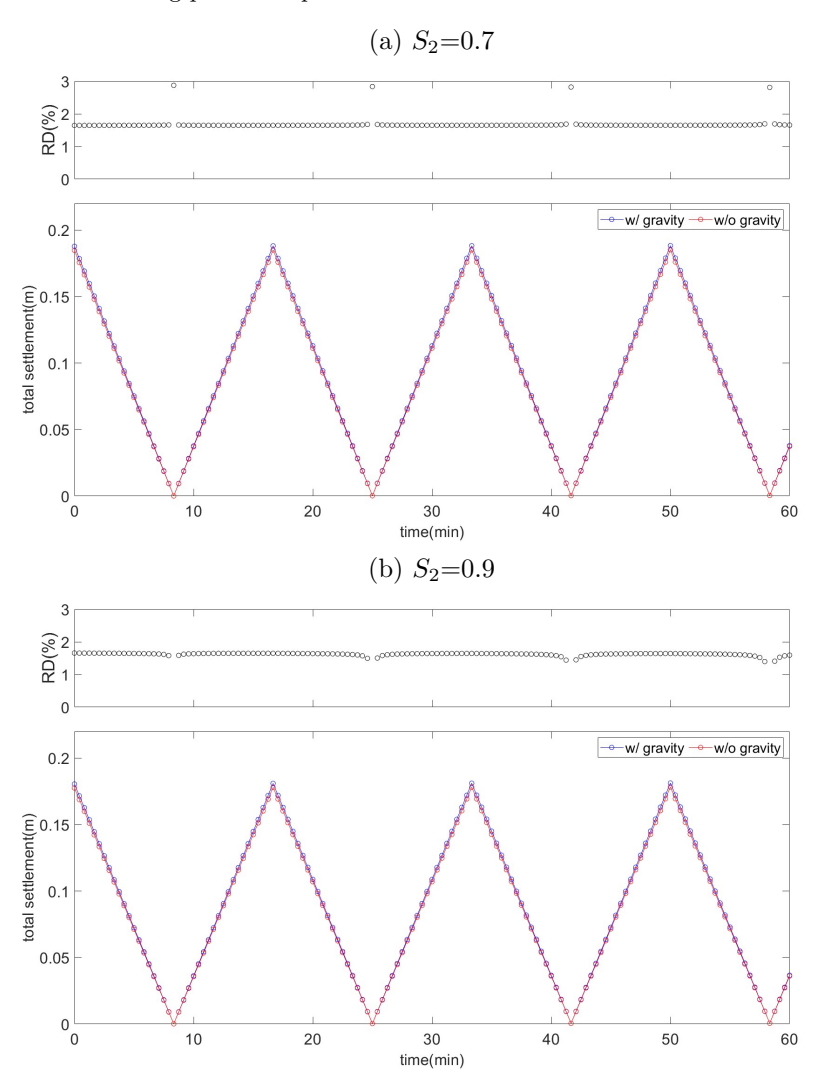


Fig. 15. Variations in the relationship between the total settlement and elapsed time (t) for an unsaturated sandy soil (h=100 m, $\omega=0.001$ Hz) for (a) $S_2=0.7$ and (b) $S_2=0.9$ due to gravity forces as well as the relative difference (RD).